

Kilogram-scale one-pot synthesis of multicomponent fullerene composites for efficient inverted perovskite solar cells

Received: 6 September 2025

Accepted: 17 February 2026

Published online: 12 March 2026

 Check for updatesEnlong Hou^{1,4}, Shuo Cheng^{1,4}, Song Kong^{2,4}, Yujue Qiu³, Jingfu Chen¹, Xingyu Chen¹, Shanshan Chen¹, Yiming Xing¹, Jinxin Yang¹, Liqiang Xie¹, Xinjing Zhao¹, Tongle Bu²✉, Zhanhua Wei¹✉ & Chengbo Tian¹✉

The high cost and detrimental self-aggregation of conventional single-component fullerenes such as C₆₀ and PCBM constitute a major obstacle to the commercialization of inverted perovskite solar cells (IPSCs). We report a kilogram-scale, one-pot synthesis of a multi-component fullerene composite (FC), comprising C₆₀, a bis((3-methyloxetan-3-yl)methyl) malonate-C₆₀ mono-adduct (BCM), and its bis-adduct (BCB). FC is obtained in 96% yields without complex column chromatography, significantly reducing production costs. Upon thermal annealing, BCM and BCB undergo cross-linking to form a robust encapsulation network that homogeneously incorporates C₆₀, enhancing film stability and electron mobility. IPSCs incorporating cross-linked fullerene composite (CFC) demonstrate an impressive efficiency of 26.55%, surpassing that of PCBM-based devices (24.82%). Additionally, CFC-based devices maintain 96.0% and 95.1% of their initial efficiency after 1000 hours under ISOS-L-1 and ISOS-D-2 protocols, respectively. Notably, CFC demonstrates excellent performance across a range of device configurations, including wide-bandgap (1.68 eV and 1.77 eV) cells, large-area devices (1 cm²), and mini-modules (14.4 cm²).

Perovskite materials have garnered significant attention in the field of solar cells due to their high absorption coefficient^{1–3}, long carrier lifetimes^{4,5}, and excellent defect tolerance⁶. Inverted perovskite solar cells (IPSCs) employing fullerene-based electron transport layers (ETLs) offer distinct advantages such as negligible hysteresis⁷, high power conversion efficiency^{8–13}, continuously improving long-term operational stability^{14–18}, and compatibility with tandem architectures^{19–22}, making them one of the most promising perovskite photovoltaic technologies for industrialization. A critical challenge limiting their commercial-scale deployment, as universally acknowledged by both academia and industry, lies in the instability of

conventional electron transport layers (ETLs)²³. Fullerenes, particularly C₆₀ and (6,6)-phenyl-C₆₁-butyric acid methyl ester (PCBM), have been extensively employed as ETLs in IPSCs due to their excellent electron extraction capabilities and suitable energy level alignment with perovskite absorbers. However, these single-component fullerenes suffer from severe self-aggregation under continuous illumination, which has been conclusively linked to their poor long-term stability and identified as a primary barrier to commercial-scale implementation, as demonstrated by recent collaborative studies between academic laboratories and industrial manufacturers^{24,25}. The aggregation-induced interfacial defects facilitate ion migration from the

¹Xiamen Key Laboratory of Optoelectronic Materials and Advanced Manufacturing, Institute of Luminescent Materials and Information Displays, College of Materials Science and Engineering, Huaqiao University, Xiamen, China. ²State Key Laboratory of Advanced Technology for Materials Synthesis and Processing, Wuhan University of Technology, Wuhan, P.R. China. ³State Key Laboratory of Physical Chemistry of Solid Surfaces, College of Chemistry and Chemical Engineering, Xiamen University, Xiamen, China. ⁴These authors contributed equally: Enlong Hou, Shuo Cheng, Song Kong.

✉ e-mail: tongle.bu@whut.edu.cn; weizhanhua@hqu.edu.cn; cbtian@hqu.edu.cn

perovskite layer, accelerating device degradation and compromising operational reliability^{26–28}. Therefore, dense and stable fullerene-based ETLs are essential for ensuring the overall stability of IPSCs.

Cross-linking is widely recognized as a key strategy for designing robust and stable films across various research fields^{29,30}. In IPSCs, several cross-linkable fullerene derivatives have been reported as ETLs or electron extraction layers to improve device stability. For instance, some cross-linkable fullerenes, MPMIC₆₀, [6,6]-phenyl-C₆₁-butyric styryl dendron ester (PCBSD), and phenyl-C₆₁-butyric acid benzocyclobutene ester (PCBCB), as replacements for PCBM and C₆₀, resulting in improved device stability^{31–33}. However, these cross-linkable fullerenes typically require high temperatures of at least 150 °C to form cross-linked films, which can damage the perovskite (PVSK) layer, limiting their application in IPSCs. Our recent study addressed this issue by discovering that C₆₀ functionalized with bis(3-methyloxetan-3-yl)methyl malonate can undergo cross-linking at a significantly lower temperature of 100 °C³⁴. This not only prevents damage to the PVSK layer but also enables functional groups to chemically interact with the PVSK, further enhancing device stability. Integrating these multiple functions into a single molecule typically requires sophisticated functional-group design, laborious purification steps, and high synthesis costs, making such an “all-in-one” architecture considerably challenging. Meanwhile, researchers have also explored blending various fullerene derivatives to cooperatively enhance performance^{35,36}. However, the synthesis and purification costs of the relevant derivatives remain prohibitively high, which hinders their potential for scalable application.

In this study, we move beyond the pursuit of a single “perfect molecule” and instead develop a fullerene composite (FC) prepared via a one-pot, kilogram-scale process for use as the ETL in IPSCs. The one-pot synthesis eliminates the need for costly separation and purification steps, delivers a yield as high as 96%, and significantly reduces material production costs. Unlike conventional single-component fullerenes, FC consists of C₆₀, bis(3-methyloxetan-3-yl)methylmalonate-C₆₀ monoadduct (BCM), and bis(3-methyloxetan-3-yl)methyl malonate-C₆₀ bisadduct (BCB). Thermal annealing at 100 °C triggers cross-linking of BCM and BCB to form a robust network, while C₆₀ is confined within this network. The three components act synergistically, enabling efficient electron transport while markedly enhancing the long-term stability of the film. The resulting cross-linked multi-component fullerene composite (CFC) exhibits favorable energy level alignment with perovskite absorbers, high electron mobility, and exceptional resistance to ion migration. IPSCs incorporating CFC ETL yield an impressive efficiency of 26.55%, surpassing that of PCBM-based devices (24.82%). Notably, CFC-based devices maintain 96.0 and 95.1% of their initial efficiency after 1000 h under ISOS-L-1 and ISOS-D-2 protocols, respectively, showcasing their exceptional operational stability. Furthermore, CFC-based ETLs demonstrate high efficiency and long-term operational stability across large-area devices (1 cm²), 14.4 cm² mini-modules, and wide-bandgap devices (1.68 eV and 1.77 eV). This work highlights FC as a scalable and commercially viable ETL, advancing the industrialization of high-performance perovskite photovoltaics.

Results

Kilogram-scale fullerene composite synthesis

The FC was synthesized via a Bingle reaction between bis(3-methyloxetan-3-yl)methyl malonate (BOM) and C₆₀ (Fig. 1a). By adjusting the reaction time, three different FCs with varying component ratios were obtained (FC1, FC, and FC3). Specifically, the reaction times for FC1, FC, and FC3 were 10, 20, and 30 h, respectively. Using our custom-designed scaled-up reaction apparatus, kilogram-scale fullerene products can be readily obtained (Fig. 1b). This result highlights the excellent scalability of the reaction and underscores its strong potential for practical and industrial applications. The presence of C₆₀,

BCM, and BCB components was confirmed using matrix-assisted laser desorption/ionization time-of-flight mass spectrometry (MALDI-TOF-MS) (Supplementary Fig. 1). The molar ratios of the components are as follows: for FC1, the proportions of C₆₀, BCM, and BCB are 44%, 39%, and 17%, respectively; for FC, the proportions are 27%, 50%, and 23%; and in FC3, the proportions are 21%, 41%, and 38% (Fig. 1c). The reproducibility of the ternary composition was confirmed by HPLC (Supplementary Fig. 2). The yields of the FCs obtained at different reaction times are provided in Supplementary Table 1. The FC achieved a high yield of up to 96%, and a commercial-scale cost analysis indicates that the synthesis cost of FC is significantly lower than that of the widely used commercial PCBM (Supplementary Tables 2 and 3). We then fabricated IPSC (device structure: ITO/HTL/PVSK/ETL/BCP/Ag, Supplementary Fig. 3) using these various ETLs. As depicted in Fig. 1d and summarized in Supplementary Table 4, devices incorporating CFC ETL exhibited superior efficiencies compared to those using PCBM and binary mixtures of FC (Supplementary Fig. 4). Statistical data on device performance (Supplementary Fig. 5) indicate that CFC-based devices show significant improvements in open-circuit voltage (V_{oc}), short-circuit current density (J_{sc}), and fill factor (FF) relative to PCBM-based devices. Notably, the device using CFC achieved an efficiency of 26.55%, surpassing the performance of devices with PCBM (24.82%) and those with CFC1 and CFC3 (Fig. 1e). Furthermore, the forward and reverse scan data demonstrate that IPSCs based on CFC exhibit reduced hysteresis compared to those based on PCBM (Supplementary Fig. 6 and Supplementary Table 5). The device performance also demonstrates high robustness against variations in the CFC layer thickness (Supplementary Fig. 7).

We also evaluated the stability of the devices under maximum power point (MPP) tracking conditions with one sun illumination. As shown in Fig. 1f, the unencapsulated device based on CFC maintained 96.0% of its initial efficiency after 1000 h under the ISOS-L-1 protocol, whereas the PCBM-based device preserved only 47.9% of its initial efficiency. Additionally, we assessed the thermal stability of the devices. The CFC-based device retained 95.1% of its initial efficiency after 1000 h of aging under the ISOS-D-2 protocol at 85 °C, while the PCBM-based device maintained only 66.7% of its initial efficiency (Fig. 1g). Meanwhile, the CFC-based devices demonstrated superior ambient storage stability compared to the PCBM-based devices. (Supplementary Fig. 8).

Film characteristics of the fullerene composite

To understand the reasons behind the changes in device stability, we employed time-of-flight secondary ion mass spectrometry (ToF-SIMS) to track the distribution of Ag⁺, Ag₂I⁺, C₆₀⁺, Pb⁺, and FA⁺ ions in PCBM- and CFC-based devices before and after 1000 h of MPP tracking. As shown in Fig. 2a and Supplementary Fig. 9, the electrodes of the PCBM-based devices exhibited significant darkening, indicating severe corrosion. A large quantity of Ag⁺ ions was detected in the PCBM and PVSK layers, and FA⁺, Pb⁺, and Ag₂I⁺ species were specifically identified in the silver electrode. This suggests that the PCBM ETL is unstable under long-term operational conditions, allowing ions such as FA⁺, Pb²⁺, and I⁻ from the PVSK to penetrate the PCBM layer and reach the silver electrode, resulting in electrode corrosion and PVSK degradation. Cross-sectional scanning electron microscope (SEM) images of the device after 1000 h of MPP tracking (Supplementary Fig. 10) showed significant aggregation in the PCBM film and noticeable changes in the PVSK phase. X-ray diffraction (XRD) patterns (Supplementary Fig. 11) presented a significant increase in the PbI₂ peak in the PVSK film with PCBM as the ETL, indicating substantial degradation of the PVSK. In contrast, in CFC-based devices, FA⁺ and Pb⁺ ions were mainly accumulated in the PVSK layer, with no apparent corrosion observed on the electrodes (Fig. 2b). This observation suggests that the CFC layer effectively blocks ion diffusion from the PVSK layer to the silver electrode, reducing electrode corrosion and PVSK degradation.

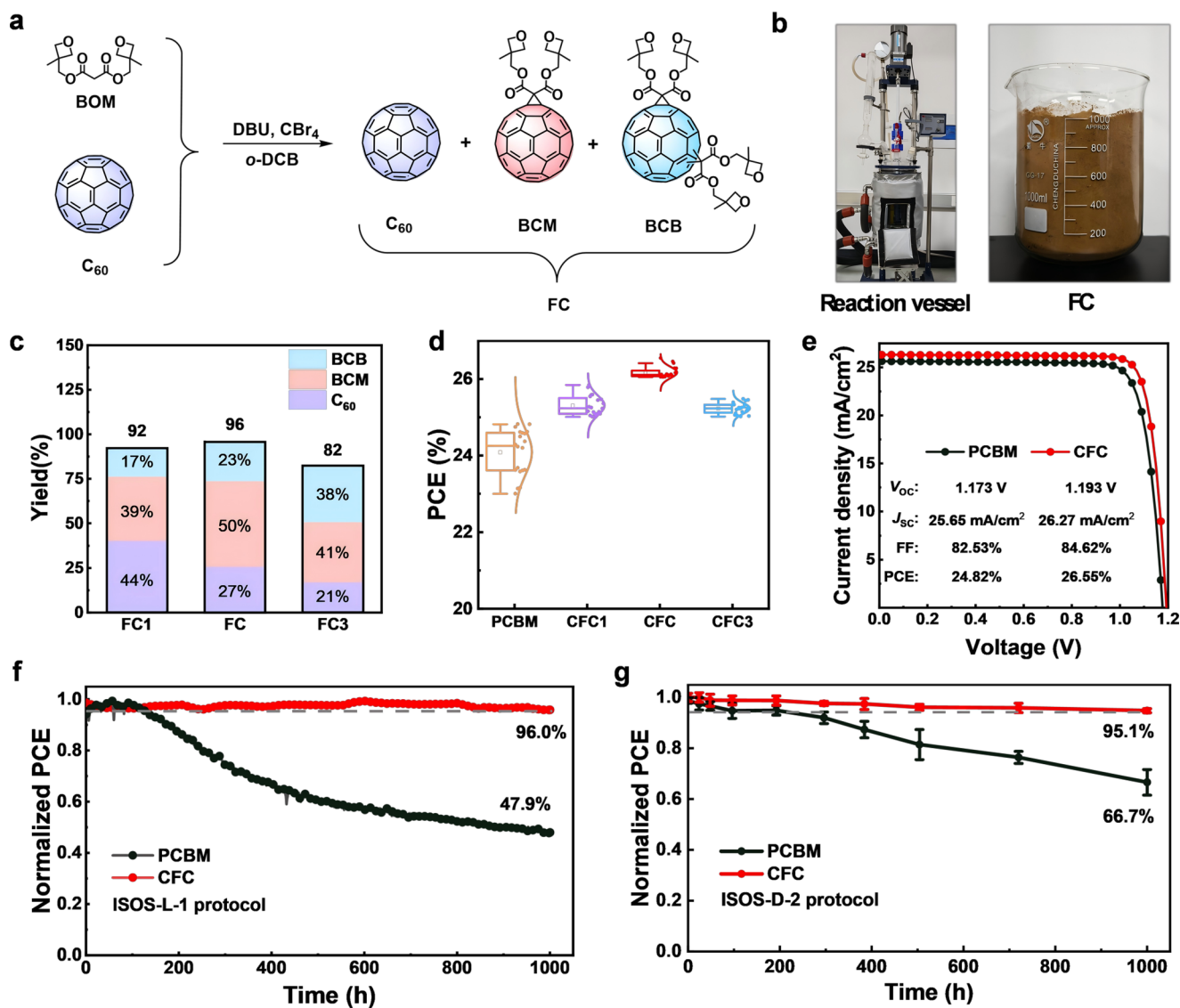


Fig. 1 | Kilogram-scale fullerene composite synthesis. **a** Synthetic route of FC. **b** Scaled-up reaction vessel and kilogram-scale product. **c** Yield of FCs at different reaction times and the composition percentage of each component. **d** Statistical analysis of device efficiency with different ETLs, the boxes show the 25th and 75th percentiles, and the whiskers display the 5th and 95th percentiles. The median and

mean are indicated by the dividing lines across the boxes and the open square symbols, respectively. **e** *J*-*V* curves of the devices with different ETLs. **f** Device stability under one sun illumination according to the ISOS-L-1 protocol. **g** Device stability at 85 °C for PCBM- and CFC-based devices under the ISOS-D-2 protocol, and the data is plotted with standard deviations (SD).

Additionally, cross-sectional SEM images showed that the CFC film maintained its intact structure, and the PVSK layer preserved its morphology throughout the same MPP tracking period, with no significant changes observed in the XRD patterns of the PVSK phase. Based on these findings, we attribute the improved device stability to the compact and stable CFC-based ETL, which effectively eliminates molecular aggregation and reduces ion diffusion from the PVSK to the silver electrode.

To further elucidate the mechanism underlying the enhanced device stability, we prepared FC film from chlorobenzene solution and found that, after heating at 100 °C (Fig. 2c), it became insoluble in chlorobenzene, indicating that FC undergoes cross-linking at this temperature. The results from annealing-time-dependence and solvent-resistance tests on the CFC film (Supplementary Figs. 12 and 13) reveal that an 8-min annealing step is sufficient to induce the formation of a stable cross-linked fullerene film. X-ray photoelectron spectroscopy (XPS) revealed that the C-O peak shifted from 533.9 eV before annealing to 534.1 eV after annealing (Supplementary Fig. 14), consistent with oxetane-ring opening and cross-link

formation. Fourier-transform infrared spectroscopy (FTIR) further supported this conclusion, as the characteristic oxetane absorption peak at 983 cm⁻¹ disappeared after annealing (Supplementary Fig. 15). In accelerated aging tests involving continuous annealing at 100 °C, optical microscopy images (Fig. 2d, e) revealed pronounced granular aggregation in PCBM films after 200 h, indicating significant self-aggregation. In contrast, CFC films showed no noticeable changes before and after aging, confirming their superior thermal stability.

The compactness of the functional layer is crucial for the stability of PVSK devices. To evaluate this, we measured the densities of CFC and PCBM films using the Beer-Lambert law. First, we measured the absorbance of FC and PCBM films at different concentrations (Supplementary Fig. 16) and established the relationship between absorbance and concentration (Supplementary Fig. 17). Using the UV-visible (UV-Vis) spectra of dissolved films solution and the thickness variation from FC to CFC films (Supplementary Fig. 18), the densities of CFC and PCBM films were calculated to be 1.0670 and 0.8427 g/cm³, respectively (Fig. 2f). Additionally, we monitored the changes in water contact angle over time for different fullerene ETLs (Supplementary

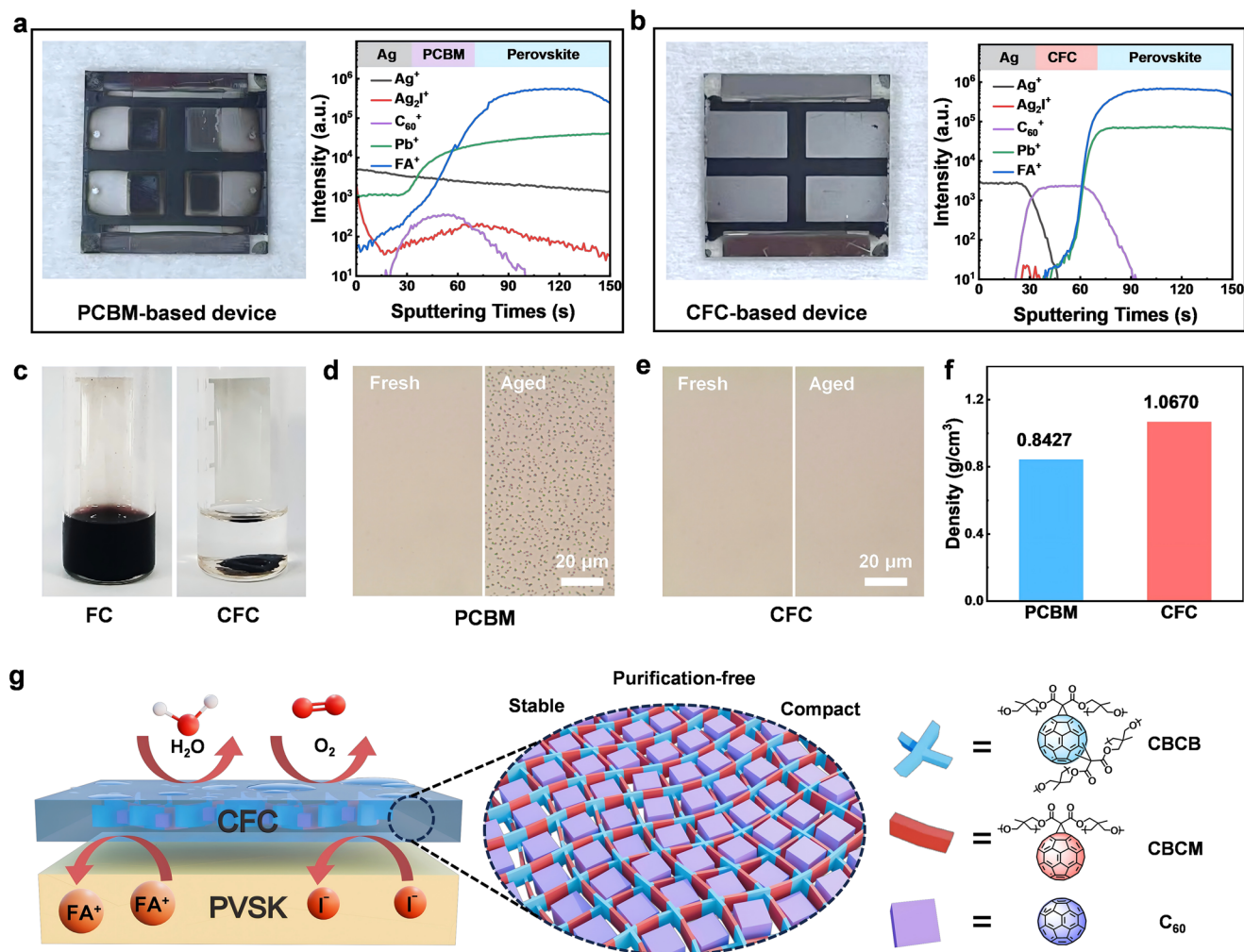


Fig. 2 | Film characteristics of the fullerene composite. **a, b** Photographs of the electrodes and TOF-SIMS measurements of PCBM- and CFC-based devices after 1000 h of MPP tracking. **c** Images of FC and CFC in chlorobenzene. **d, e** Polarized optical microscope images of PCBM and CFC films on glass before and after 200 h

of thermal aging at 100 °C. **f** Film density comparison between PCBM- and CFC-based ETLs. **g** Schematic illustration of the CFC ETL, which is formed via the synergistic combination of C₆₀ and cross-linkable fullerenes.

Fig. 19), revealing that CFC-based films exhibited superior hydrophobicity and stability. These findings suggest that dense and stable CFC films not only protect PVSK from water and oxygen erosion but also effectively prevent ion diffusion from the PVSK to the metal electrode, thereby enhancing device stability.

Building on the exceptional properties of CFC, we propose a schematic diagram to illustrate its functional mechanism (Fig. 2g). The cross-linkable fullerene components (BCM and BCB) within CFC undergo synergistic cross-linking to form a robust network that effectively encapsulates and stabilizes C₆₀. This strategy enables the formation of a low-cost, high-density fullerene composite ETL with improved electron mobility and stability, thereby promoting the fabrication of highly efficient and stable IPSCs.

Enhanced charge transport in the fullerene composite

Proper energy level alignment with PVSKs and high electron mobility are also crucial for fullerene-based ETLs. We characterized the band structure of fullerene films using ultraviolet photoelectron spectroscopy (UPS) and UV-Vis absorption spectroscopy. As shown in Fig. 3a, the valence band maxima (E_{VBM}) for CFC and PCBM films were determined to be -5.65 and -5.66 eV, respectively. Combining these results with UV-Vis absorption spectra (Supplementary Fig. 20), the conduction band minima (E_{CBM}) for CFC and PCBM films were calculated to be -3.90 and -3.93 eV, respectively (Fig. 3b and Supplementary

Table 6). These results indicate favorable energy-level alignment between CFC and the perovskite absorber, as further confirmed by KPFM measurements (Supplementary Fig. 21). We also fabricated electron-only devices with an ITO/Al/Fullerene/Al structure and recorded the I-V curves under dark conditions. As shown in Fig. 3c, the electron mobility of the CFC film was calculated to be $4.02 \times 10^{-4} \text{ cm}^2 \text{ V}^{-1} \text{ s}^{-1}$, which is higher than that of PCBM ($1.76 \times 10^{-4} \text{ cm}^2 \text{ V}^{-1} \text{ s}^{-1}$). This indicates that the CFC film demonstrates superior electron transport capability compared to PCBM films.

The interfacial interactions between the ETL and PVSK facilitate efficient carrier extraction and defect passivation^{37,38}. In the X-ray photoelectron spectroscopy (XPS) of PVSK/CFC films (Fig. 3d), the Pb 4f peak shifts towards lower binding energies, suggesting a coordination interaction between the C=O groups in CFC and Pb²⁺. Further confirmation of this interaction is provided by FTIR measurements, where the C=O stretching peak of CFC shifts from 1749.6 to 1738.5 cm^{-1} upon mixing with PbI₂ (Supplementary Fig. 22), in agreement with the XPS results (Supplementary Fig. 23). Theoretical calculations indicate that the PVSK/CFC interface exhibits stronger interactions and more effective defect passivation compared to PVSK/PCBM. (Supplementary Fig. 24). We therefore evaluated the trap density using the SCLC method. As shown in Fig. 3e, the trap-filled limit voltages (V_{TFL}) of the devices based on PCBM and CFC were 0.191 and 0.098 V , respectively, corresponding to trap densities of $9.90 \times 10^{14} \text{ cm}^{-3}$ and $5.08 \times 10^{14} \text{ cm}^{-3}$

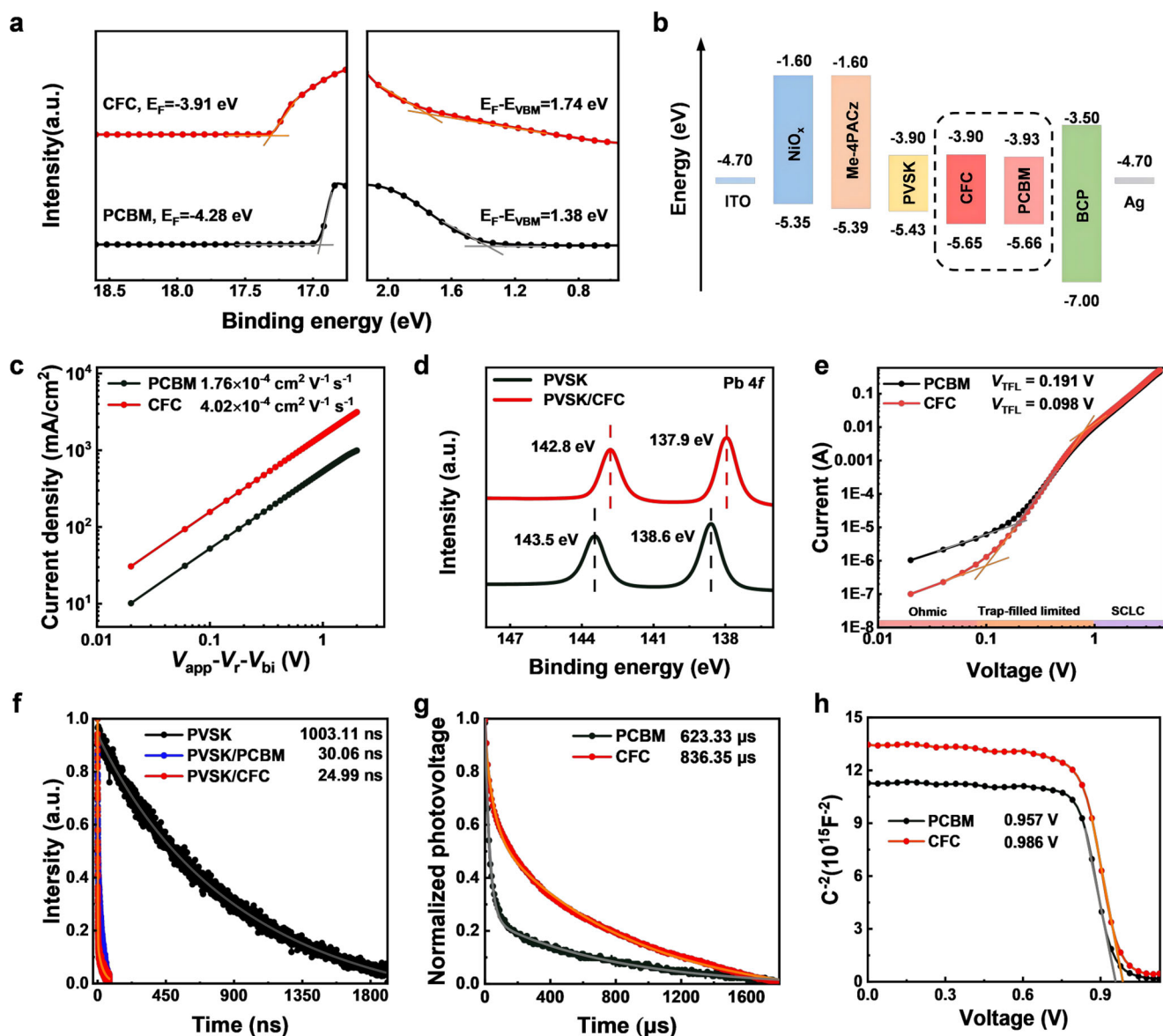


Fig. 3 | Enhanced charge transport in the fullerene composite. **a** UPS spectra of CFC and PCBM. **b** Energy level diagram of NiO_x , Me-4PACz, PVS, CFC, PCBM, and BCP. **c** Electron mobility measurement of PCBM- and CFC-based films. **d** XPS spectra of Pb 4f for PVS and CFC/PVS. **e** I-V curves of the electron-only device

with the structure of ITO/ SnO_2 /perovskite/ETL/Ag. **f** TRPL spectra of PVS and PVS coated with different ETLs. **g** Normalized TPV curve and **h** Mott-Schottky plots of different IPSCs.

(detailed calculations in Supplementary Note 2). The significant reduction in trap density indicates that CFC can effectively passivate surface defects in PVS films.

The influence of charge transfer and recombination dynamics at the PVS/ETL interface was further investigated through time-resolved photoluminescence (TRPL) and steady-state photoluminescence (PL) measurements. Figure 3f shows the TRPL spectra of PVS films and PVS films covered with different ETLs. The data, fitted with a biexponential function, reveal average PL lifetimes for PVS, PVS/PCBM, and PVS/CFC films of 1003.11, 30.06, and 24.99 ns, respectively (Supplementary Table 7). The significant reduction in PL lifetime for PVS films with an ETL suggests rapid electron extraction at the PVS/ETL interface. Furthermore, the shorter PL lifetime for CFC compared to PCBM indicates a higher electron extraction efficiency. Additionally, the τ_2 value for PVS/CFC (34.12 ns) is greater than that of PVS/PCBM (31.35 ns), which suggests a reduced density of defect states, in agreement with the trap density measurements. The PL results also show that PVS films coated with CFC exhibit the lowest PL intensity,

further confirming the effective electron extraction capability of CFC (Supplementary Fig. 25).

Moreover, transient photovoltage (TPV) and transient photocurrent (TPC) measurements were performed to study charge transfer and recombination mechanisms in the corresponding devices. As shown in Fig. 3g and Supplementary Table 8, the TPV decay lifetime for CFC-based device is 836.35 μs , which is longer than that of PCBM-based device (623.33 μs). Meanwhile, the TPC decay lifetimes for devices based on PCBM and CFC are 14.88 and 4.54 μs , respectively (Supplementary Fig. 26 and Supplementary Table 9). The significantly shorter lifetime of the CFC-based device corresponds to faster charge extraction and transport, which accounts for its higher J_{SC} . Figure 3h presents the Mott-Schottky plots for devices based on PCBM and CFC. The built-in potential (V_{bi}) for PCBM-based devices is 0.957 V, while that for CFC-based devices is 0.986 V. The higher V_{bi} in CFC devices facilitates carrier extraction and transfer within the device, which helps explain the higher V_{OC} observed in CFC-based devices. Additionally, the ideality factor calculated from V_{OC} as a function of different

incident light intensities decreases from 1.79 kT/q in PCBM-based devices to 1.48 kT/q in CFC-based devices (Supplementary Fig. 27), indicating effective suppression of defect-induced non-radiative recombination. Electrochemical impedance spectroscopy (EIS) results (Supplementary Fig. 28) also show a larger charge recombination resistance (R_{rec}) in CFC-based devices, further confirming the effective suppression of non-radiative recombination.

Wide bandgap inverted perovskite solar cell performance

To investigate the applicability of the CFC, we fabricated IPSCs with a 1.68 eV bandgap PVSK absorber, using an ITO/HTL/PVSK/CFC/BCP/Ag structure. As shown in Fig. 4a, the CFC-based 1.68 eV bandgap IPSC achieved a champion efficiency of 23.16%, featuring a V_{OC} of 1.263 V, a J_{SC} of 21.81 mA/cm², and a fill factor (FF) of 84.08% (Supplementary Fig. 29 and Supplementary Table 10). In comparison, the PCBM-based device exhibited a significantly lower efficiency of 21.21%. Additionally, the CFC-based device exhibits reduced hysteresis (Fig. 4b), achieving a

steady-state efficiency of 23.14% (Fig. 4c). We further fabricated IPSCs using a 1.77 eV bandgap PVSK absorber (Fig. 4d). Compared with the PCBM-based device, which achieves a PCE of 18.77%, the CFC-based device demonstrated notable enhancements in V_{OC} , J_{SC} , and FF (Supplementary Fig. 30 and Supplementary Table 11), resulting in a PCE of 20.39% with negligible hysteresis (Fig. 4e) and a steady-state PCE of 20.37% (Fig. 4f). The external quantum efficiency (EQE) spectra of the devices are shown in Supplementary Fig. 31, and the integrated J_{SC} values are in good agreement with those derived from the J - V measurements. Their efficiencies are comparable to those of the high-performance 1.68 and 1.77 eV bandgap IPSCs currently reported (Supplementary Tables 12 and 13).

The stability of the device with a 1.68 eV bandgap PVSK absorber under the ISOS-L-1 protocol is depicted in Fig. 4g. The unencapsulated CFC-based device retains 95.1% of its initial efficiency after 1000 h. Similarly, the device with a 1.77 eV bandgap PVSK absorber maintains 95.4% of its initial efficiency under the same conditions (Fig. 4h).

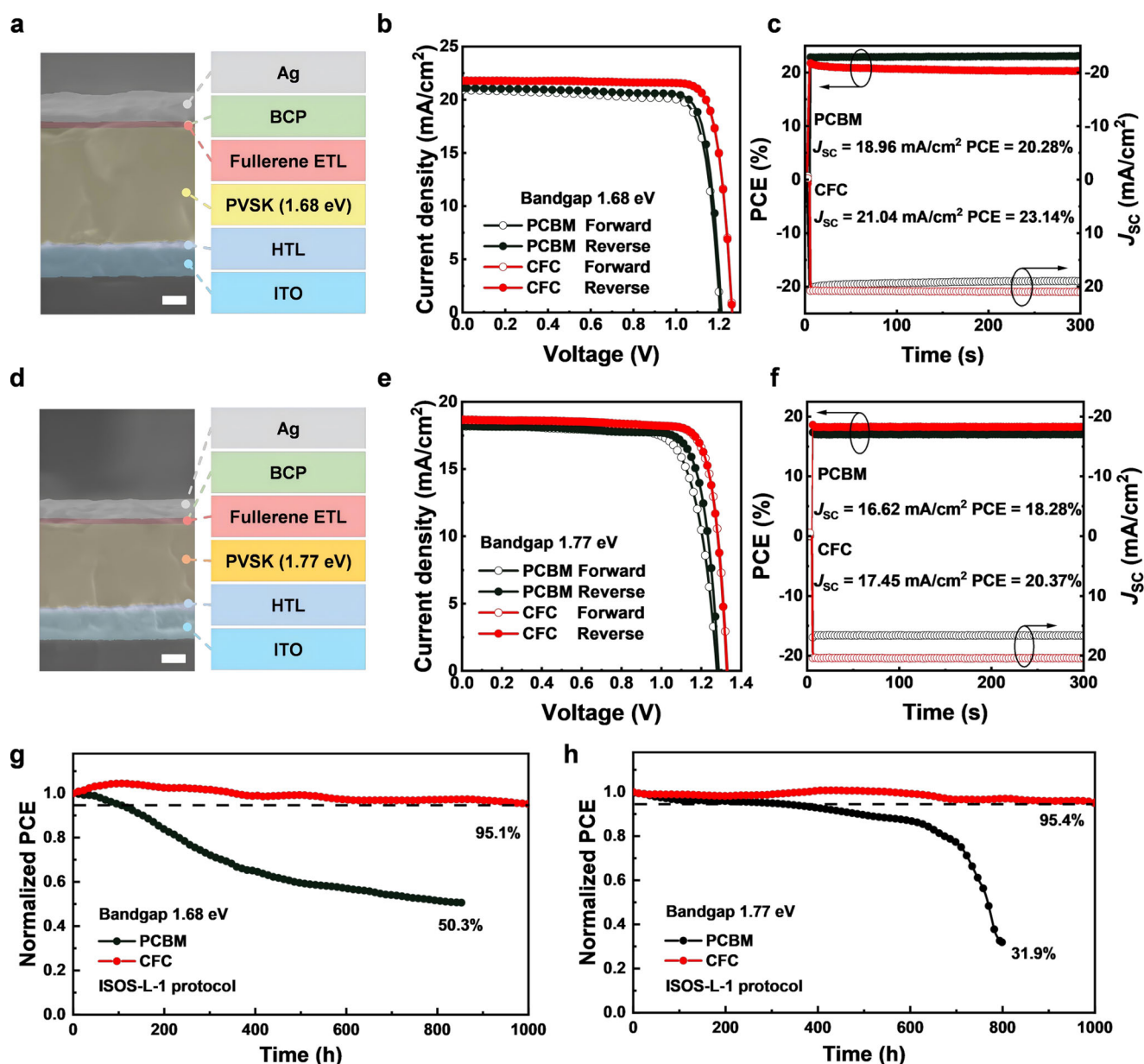


Fig. 4 | Wide bandgap inverted perovskite solar cell performance. **a** Device structure of 1.68 eV bandgap IPSCs, (scale bar: 100 nm). **b, c** J - V curves and Steady-state output efficiency of 1.68 eV bandgap IPSCs with different ETLs. **d** Device

structure of 1.77 eV bandgap IPSCs, (scale bar: 100 nm). **e, f** J - V curves and Steady-state output efficiency of 1.77 eV bandgap IPSCs with different ETLs. **g, h** ISOS-L-1 stability of 1.68 and 1.77 eV bandgap IPSCs under one sun illumination.

Notably, under the ISOS-L-1 protocol, the CFC-based devices outperform their PCBM-based counterparts, suggesting that CFC not only improves efficiency but also enhances the operational stability of IPSCs across different bandgaps. These results demonstrate the versatility of CFC across perovskite solar cells with diverse compositions and suggest its relevance for scalable device fabrication.

Scalable photovoltaic performance of devices and mini-modules

To assess the performance of CFC across different scales, we fabricated both 1 cm² single cells and 14.4 cm² mini-modules. At the 1 cm² scale, the champion CFC-based device achieved an efficiency of 25.36%, with a V_{OC} of 1.191 V, a J_{SC} of 26.02 mA cm⁻², and an FF of

81.85%, outperforming the PCBM-based device (24.08%) (Fig. 5a). The advantage is further confirmed by the steady-state output efficiencies of 25.13% for CFC-based device versus 23.96% for PCBM-based device (Fig. 5b and Supplementary Table 14). Additionally, the CFC devices also demonstrated superior device-to-device reproducibility (Fig. 5c and Supplementary Fig. 32).

For the 14.4 cm² mini-modules, CFC exhibited significant advantages. The champion CFC-based mini-module reached an efficiency of 23.81%, higher than the 22.17% of the PCBM-based counterpart, and showed a negligible hysteresis (Fig. 5d and Supplementary Table 15). This trend was further validated by the steady-state output efficiency measured near the MPP. The CFC-based mini-module stabilized at

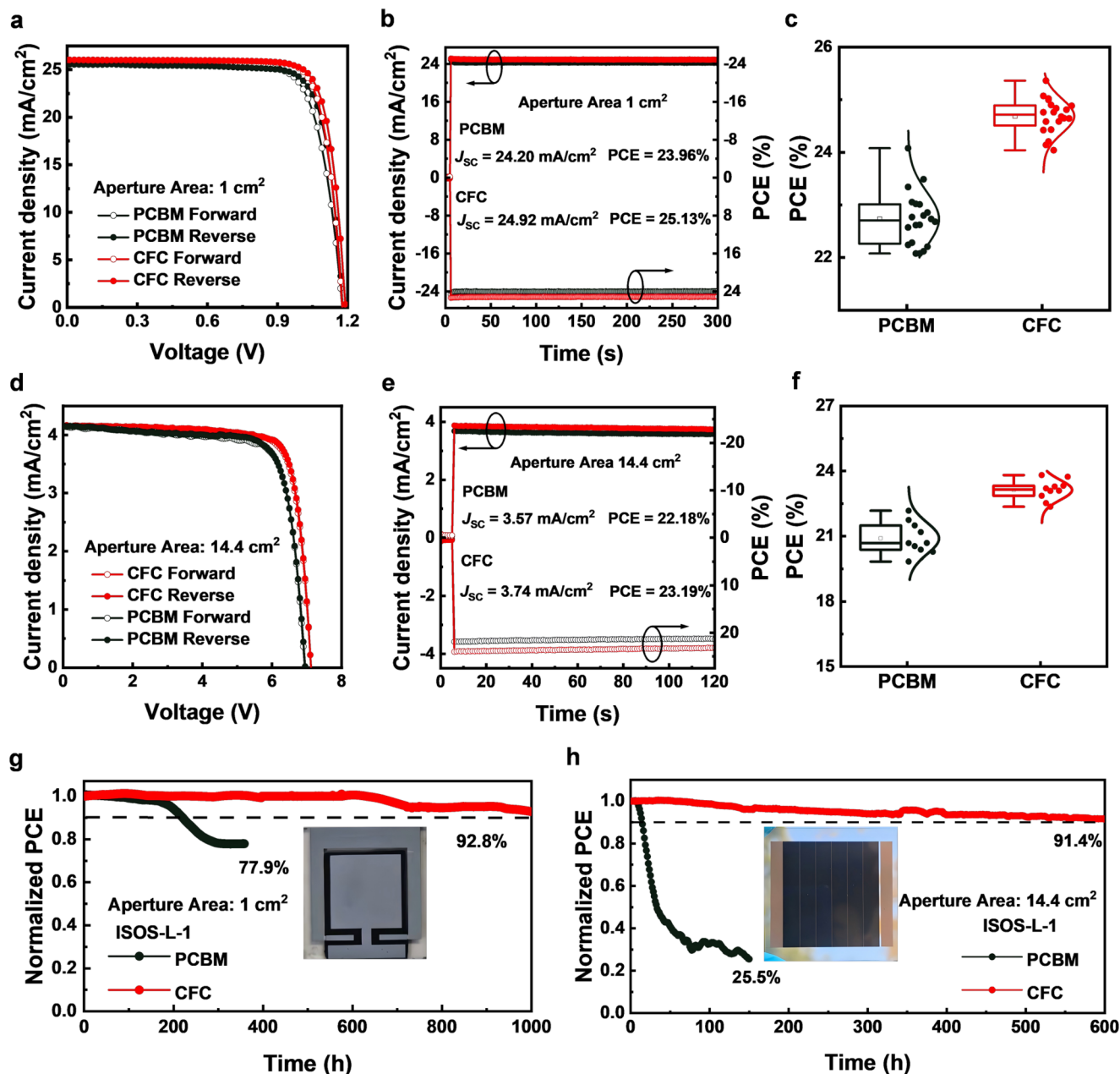


Fig. 5 | Scalable photovoltaic performance of devices and mini modules. **a–c** Performance of 1 cm² devices. **a** forward/reverse J - V curves; **b** steady-state output at the MPP; **c** PCE statistics. **d–f** Performance of 14.4 cm² mini-modules. **d** forward/reverse J - V curves; **e** steady-state output at the MPP; **f** PCE statistics. In **c** and **f**, the boxes show the 25th and 75th percentiles, and the whiskers display the 5th and 95th

percentiles. The median and mean are indicated by the dividing lines across the boxes and the open square symbols, respectively. **g**, **h** Photographs of the 1 cm² device and the 14.4 cm² mini-module, and their operational stability under continuous MPP tracking.

23.19% over 120 s, compared to 22.18% for the PCBM-based device (Fig. 5e), which is consistent with the J - V scan results. Moreover, the CFC-based mini-modules displayed a narrower PCE distribution, indicating better performance uniformity after device scaling (Fig. 5f). The corresponding distributions of V_{OC} , J_{SC} , and FF are provided in Supplementary Fig. 33.

We further assessed the long-term operational stability of both 1 cm^2 devices and 14.4 cm^2 mini-modules through MPP tracking. The 1 cm^2 CFC-based device retained 92.8% of its initial efficiency after 1000 h (Fig. 5g), while the PCBM-based device degraded to 77.9% within 400 h. Similarly, the 14.4 cm^2 CFC-based mini-module maintained 91.4% of its initial efficiency after 600 h (Fig. 5h), whereas the PCBM-based device rapidly declined to 25.5% within just 200 h. These results collectively demonstrate that the stability advantage of CFC is preserved under both area upscaling and prolonged operational conditions.

Discussion

We introduce a paradigm shift from the pursuit of a single “perfect” molecular material toward a rationally designed multicomponent, functionally cooperative system. Through a facile, scalable one-pot synthesis, we construct a ternary fullerene composite (FC) comprising C_{60} , mono-adduct, and bis-adduct fullerenes, wherein each component plays a distinct yet synergistic role. The resulting CFC film, formed via low-temperature cross-linking at $100\text{ }^\circ\text{C}$, enables a champion efficiency of 26.55% in IPSCs, outperforming conventional PCBM-based devices (24.82%). Remarkably, CFC-based devices exhibit excellent operational stability, retaining 96.0% (ISOS-L-1) and 95.1% (ISOS-D-2) of their initial efficiency after 1000 h. These improvements are attributed to a homogeneous, immobilized C_{60} network that ensures efficient electron transport while mitigating perovskite degradation under prolonged operation. More importantly, CFC demonstrates remarkable processing robustness and material universality, as evidenced by the performance advantage upon scaling to 14.4 cm^2 mini-modules and its effective extension to wide-bandgap perovskites (1.68 and 1.77 eV), highlighting its potential as an efficient and stable ETL for inverted perovskite photovoltaics.

Methods

Materials

N, N-dimethylformamide (DMF, 99.8%), dimethyl sulfoxide (DMSO, 99.9%), 2-propanol (IPA, anhydrous, 99.5%), chlorobenzene (anhydrous, 99.8%), anisole (anhydrous, 99.7%), and cesium iodide (CsI, 99.9%) were purchased from Sigma Aldrich. Lead iodide (PbI_2 , 98%) and [4-(3,6-Dimethyl-9H-carbazol-9-yl)butyl]phosphonic acid (Me-4PACz, >99.0%) were purchased from TCI. Methylammonium iodide (MAI, 98.0%) and formamidinium iodide (FAI, 99.99%) were purchased from Greatcell Solar. Lead chloride (PbCl_2 , 99.9%) and methylammonium chloride (MACl, 95%) were purchased from Xi'an Polymer Light Technology Corp. C_{60} (99.5%) and (6,6)-phenyl- C_{61} butyric acid methyl ester (PCBM, 99.5%) were obtained from Liantan Technology Co., Ltd. Nickel oxide (NiO_x , 99.999%) and Bathocuproine (BCP, 99%) was purchased from Advanced Electronic Technology.

Perovskite precursor solution

1.53 eV bandgap perovskite precursor solution was prepared by mixing FAI, MAI, CsI, and PbI_2 in anhydrous DMF: DMSO = 4: 1 (v: v) according to the stoichiometric formula of $1.6\text{ M Cs}_{0.05}(\text{FA}_{0.98}\text{MA}_{0.02})_{0.95}\text{PbI}_3$, with 20 mol% MACl. The 1.3 M $\text{FA}_{0.8}\text{Cs}_{0.2}\text{Pb}(\text{I}_{0.8}\text{Br}_{0.2})_3$ 1.68 eV bandgap perovskite precursor was prepared by dissolving 178.88 mg of FAI, 419.51 mg of PbI_2 , 143.13 mg of PbBr_2 , and 67.6 mg of CsI in 1 mL mixed solvent of DMF and DMSO with a volume ratio of 3:1. For 1.77 eV bandgap perovskite precursor solution, FAI:CsI:PbBr₂:PbI₂ (molar ratio = 0.8:0.2:0.4:0.6) were dissolved in mixed DMF and DMSO solvents (volume ratio = 1:1.4) at a concentration of 1.2 M.

Device fabrication

The pre-patterned ITO glass substrates underwent a thorough cleaning process, including sonication with a cleaning agent, deionized water, IPA, and ethanol, followed by drying with high-pressure nitrogen and plasma treatment. Next, the NiO_x HTL solution was applied to the substrate via spin-coating and annealed at $100\text{ }^\circ\text{C}$ for 10 min. Following this, the Me-4PACz self-assembled molecular solution was applied to create a double-layered hole-transport layer. For the hole transport layer (HTL) solution, 10 mg/mL NiO_x was dissolved in deionized water. After shaking for 20 min, the solution was filtered through a $0.22\text{ }\mu\text{m}$ polytetrafluoroethylene membrane before use. The self-assembled molecular layer solution was prepared by dissolving 0.5 mg/mL Me-4PACz in ethanol.

Subsequently, 80 μL of perovskite precursor solution was dropped onto substrates and spun at 2000 rpm for 25 s and 5000 rpm for 30 s. 10 s before the end of the program, 150 μL of anisole was poured onto the substrates. The substrates were then transferred to an annealing stage at $100\text{ }^\circ\text{C}$ for 30 min. After cooling to room temperature, a PDAl₂ isopropanol solution (1 mg/mL) was spin-coated onto the perovskite films at 5000 rpm for 25 s, followed by annealing at $100\text{ }^\circ\text{C}$ for 5 min. Following this, the FC chlorobenzene solution (20 mg/mL) was spin-coated at 2500 rpm for 30 s on the perovskite films and annealed at $100\text{ }^\circ\text{C}$ for 10 min. Next, the BCP 2-propanol solution (0.5 mg/mL) was spin-coated at 5000 rpm for 30 s and annealed at $100\text{ }^\circ\text{C}$ for 10 min. Finally, a 100 nm of Ag electrode was deposited through a mask by thermal evaporation under a pressure of 5.5×10^{-4} Pa.

Fabrication of mini-module

Firstly, $5 \times 5\text{ cm}$ FTO glasses were etched using a picosecond laser to form P1 patterns. Prior to use, the etched glasses were cleaned and subjected to ultraviolet-ozone (UVO) treatment. Subsequently, the NiO_x , Me-4PACz, perovskite, PCBM, and BCP layers were sequentially deposited on the patterned FTO glasses in accordance with the fabrication protocols for small-size solar cells. Following the layer deposition, the samples were etched again to form P2 patterns. After evaporating the Cu electrode, a third etching step was performed to create P3 patterns, thereby completing the series connection of 6 subcells. The scribing widths of P1, P2, and P3 were approximately 55, 115, and 35 μm , respectively. The total distance between P1 and P3 was about 210 μm , and the calculated geometric fill factor was approximately 96.5%. A $5 \times 5\text{ cm}$ metal mask with an aperture area of $3.6 \times 4\text{ cm}$ was used for the I - V test of these solar mini-modules.

Device characterization

The J - V characteristics were tested using a Keithley 2400 source meter and a Xenon lamp solar simulator (Enlitech, AAA) within an N_2 -filled glove box. The tests were conducted under AM 1.5G irradiation intensity, calibrated with NREL calibrated Si solar cells equipped with infrared cut-off filters (KG-5). Measurements were taken in the range of 1.25 to -0.1 V , with a voltage step of 0.01 V and a delay time of 40 ms.

Device stability was evaluated following the ISOS-L-1 and ISOS-D-2 protocols³⁹. For the ISOS-L-1 test, unencapsulated devices were continuously exposed to a calibrated white LED light source (100 mW cm^{-2} , AM1.5G) under ambient conditions ($50 \pm 2\text{ }^\circ\text{C}$) to assess the effect of continuous illumination on device stability. For the ISOS-D-2 test, devices were stored in the dark at an elevated temperature of $85\text{ }^\circ\text{C}$ in ambient air without humidity control to evaluate their thermal stability. No encapsulation was applied during either test, and the device performance was periodically measured using a source meter under standard testing conditions. For the device operating as an LED, the external quantum efficiency was determined by measuring the absolute radiation flux using a commercial system (Guangzhou Xi Pu Optoelectronics Technology Co., Ltd.) equipped with an integrating sphere (GPS-4P-SL, Labsphere) and a QE-Pro spectrometer (Ocean Optics).

Other characterizations

Steady-state photoluminescence (PL) was recorded using an FLS1000 instrument (Edinburgh Instruments Ltd.). High-performance liquid chromatography (HPLC) measurements were performed using an LC-16P system (Shimadzu). Time-resolved photoluminescence (TRPL) was measured with a 375 nm pulsed laser (EPL-375) excitation using time-correlated single photon counting (TCSPC) equipment (FLS1000, Edinburgh Instruments Ltd.). Space-charge-limited current (SCLC) curves were collected using a Keithley 2400 instrument in the dark, with the device's dark J - V curve scanned in the range of -0.5 to 5 V, at a voltage step of 0.01 V and a delay time of 40 ms. Top-view and cross-sectional SEM images were taken using a field-emission scanning electron microscope (JEOL JSM-7610F) operating at 5 kV. X-ray diffraction (XRD) patterns were recorded using a Smart Lab X-ray diffractometer (Rigaku Corporation) with a Cu $K\alpha$ radiation source (1.54 Å), an operating voltage of 40 kV, and a current of 30 mA. Ultraviolet-visible (UV-Vis) absorption spectra were recorded using an Ocean Insight FLAME Miniature Spectrometer in an N_2 -filled glovebox. X-ray photoelectron spectra (XPS) were measured using a Thermo Fisher Scientific K-alpha⁺ instrument with an Al $K\alpha$ source, calibrated to the C 1s peak (284.8 eV). Infrared spectra (FTIR) were collected in attenuated total reflection (ATR) mode using a NICOLET iSSO FTIR spectrometer (Thermo Scientific). Incident photon-to-electron conversion efficiency (IPCE) spectra were tested using a QE-R666 system (Enlitech) in DC mode without bias to confirm the current density. The stable output of the device was measured by applying a constant voltage near the maximum power point (MPP) extracted from the J - V curve. Electrochemical impedance spectra (EIS) were obtained using a CHI660E electrochemical workstation, biased at 0.9 V in the dark. Mott-Schottky plots were monitored by varying the voltage from 0 to 1.4 V at 10 kHz using a Zahner electrochemical workstation. Dark J - V curves of the device were recorded using a Keithley 2400 source meter with a scanning range of -1.5 to 1.5 V. Ultraviolet photoelectron spectroscopy (UPS) spectra were measured using a Thermo Fisher Scientific ESCALAB Xi⁺ with a He-I α (21.22 eV) UV light source. Water-contact angle measurements were performed using a JC2000D1 contact angle measuring device from POWEREACH. Time of Flight Secondary Ion Mass Spectrometry (ToF-SIMS) measurements (ION-TOF M6) were performed with the pulsed primary ions from a Cs⁺ (2 keV) liquid-metal ion gun for the sputtering and a Bi⁺ pulsed primary ion beam for the analysis (30 keV). The optical microscope images were recorded on a DM 250 polarized optical microscope.

Data availability

The data that support the findings of this study are available within the Article and its Supplementary Information. Source data are provided with this paper.

References

- Zhang, W., Eperon, G. E. & Snaith, H. J. Metal halide perovskites for energy applications. *Nat. Energy* **1**, 16048 (2016).
- Long, G. et al. Chiral-perovskite optoelectronics. *Nat. Rev. Mater.* **5**, 423–439 (2020).
- Yin, W.-J., Shi, T. & Yan, Y. Unique properties of halide perovskites as possible origins of the superior solar cell performance. *Adv. Mater.* **26**, 4653–4658 (2014).
- Lin, Q., Armin, A., Nagiri, R. C. R., Burn, P. L. & Meredith, P. Electro-optics of perovskite solar cells. *Nat. Photon.* **9**, 106–112 (2015).
- Chu, X. et al. Surface in situ reconstruction of inorganic perovskite films enabling long carrier lifetimes and solar cells with 21% efficiency. *Nat. Energy* **8**, 372–380 (2023).
- Liu, S. et al. Imaging the long transport lengths of photo-generated carriers in oriented perovskite films. *Nano Lett.* **16**, 7925–7929 (2016).
- Deng, L.-L., Xie, S.-Y. & Gao, F. Fullerene-based materials for photovoltaic applications: toward efficient, hysteresis-free, and stable perovskite solar cells. *Adv. Electron. Mater.* **4**, 1700435 (2018).
- You, S. et al. C₆₀-based ionic salt electron shuttle for high-performance inverted perovskite solar modules. *Science* **388**, 964–968 (2025).
- Xing, Z. et al. Solubilizing and stabilizing C₆₀ with n-type polymer enables efficient inverted perovskite solar cells. *Joule* **9**, 101817 (2025).
- Chen, J. et al. Efficient tin-based perovskite solar cells with trans-isomeric fulleropyrrolidine additives. *Nat. Photon.* **18**, 464–470 (2024).
- Xiong, Z. et al. Homogenized chlorine distribution for >27% power conversion efficiency in perovskite solar cells. *Science* **390**, 638–642 (2025).
- Luo, C. et al. Engineering bonding sites enables uniform and robust self-assembled monolayer for stable perovskite solar cells. *Nat. Mater.* **24**, 1265–1272 (2025).
- Zhang, X. et al. Advances in inverted perovskite solar cells. *Nat. Photon.* **18**, 1243–1253 (2024).
- Lin, Y.-H. et al. A piperidinium salt stabilizes efficient metal-halide perovskite solar cells. *Science* **369**, 96–102 (2020).
- Ding, B. et al. Dopant-additive synergism enhances perovskite solar modules. *Nature* **628**, 299–305 (2024).
- Duan, T. et al. Chiral-structured heterointerfaces enable durable perovskite solar cells. *Science* **384**, 878–884 (2024).
- Wu, J. et al. Inhibiting interfacial nonradiative recombination in inverted perovskite solar cells with a multifunctional molecule. *Adv. Mater.* **36**, 2407433 (2024).
- Dong, B. et al. Self-assembled bilayer for perovskite solar cells with improved tolerance against thermal stresses. *Nat. Energy* **10**, 342–353 (2025).
- Wen, J. et al. Present status of and future opportunities for all-perovskite tandem photovoltaics. *Nat. Energy* **10**, 681–696 (2025).
- Liu, S. et al. Buried interface molecular hybrid for inverted perovskite solar cells. *Nature* **632**, 536–542 (2024).
- Fu, S. et al. On-demand formation of Lewis bases for efficient and stable perovskite solar cells. *Nat. Nanotechnol.* **20**, 772–778 (2025).
- Duan, L. et al. Stability challenges for the commercialization of perovskite-silicon tandem solar cells. *Nat. Rev. Mater.* **8**, 261–281 (2023).
- He, D. et al. Compacting molecular stacking and inhibiting self-aggregation in fullerene transporting layer for efficient and stable perovskite solar cells. *Angew. Chem. Int. Ed.* **64**, e202502950 (2025).
- Tian, C. et al. Efficient and stable inverted perovskite solar cells enabled by inhibition of self-aggregation of fullerene electron-transporting compounds. *Sci. Bull.* **66**, 339–346 (2021).
- Pont, S., Foglia, F., Higgins, A. M., Durrant, J. R. & Cabral, J. T. Stability of polymer:PCBM thin films under competitive illumination and thermal stress. *Adv. Funct. Mater.* **28**, 1802520 (2018).
- Chen, P. et al. Multifunctional ytterbium oxide buffer for perovskite solar cells. *Nature* **625**, 516–522 (2024).
- Ren, X. et al. Mobile iodides capture for highly photolysis- and reverse-bias-stable perovskite solar cells. *Nat. Mater.* **23**, 810–817 (2024).
- Wu, S. et al. A chemically inert bismuth interlayer enhances long-term stability of inverted perovskite solar cells. *Nat. Commun.* **10**, 1161 (2019).
- Chen, K. et al. A general bioinspired, metals-based synergic cross-linking strategy toward mechanically enhanced materials. *ACS Nano* **11**, 2835–2845 (2017).
- Wu, Y. et al. In situ crosslinking-assisted perovskite grain growth for mechanically robust flexible perovskite solar cells with 23.4% efficiency. *Joule* **7**, 398–415 (2023).

31. Watson, B. L. et al. Cross-linkable, solvent-resistant fullerene contacts for robust and efficient perovskite solar cells with increased J_{SC} and V_{OC} . *ACS Appl. Mater. Interfaces* **8**, 25896–25904 (2016).
 32. Li, M. et al. Graphdiyne-modified cross-linkable fullerene as an efficient electron-transporting layer in organometal halide perovskite solar cells. *Nano Energy* **43**, 47–54 (2018).
 33. Wojciechowski, K. et al. Cross-linkable fullerene derivatives for solution-processed n-i-p perovskite solar cells. *ACS Energy Lett.* **1**, 648–653 (2016).
 34. Hou, E. et al. Cross-linkable fullerene electron transport layer with internal encapsulation capability for efficient and stable inverted perovskite solar cells. *Angew. Chem. Int. Ed.* **64**, e202416703 (2024).
 35. Sun, H. et al. Scalable solution-processed hybrid electron transport layers for efficient all-perovskite tandem solar modules. *Adv. Mater.* **36**, 2308706 (2024).
 36. Surel, J. L. et al. Approaching the radiative limits for wide bandgap perovskite solar cells using fullerene blend electron transport interlayers. *EES Sol.* **1**, 567–579 (2025).
 37. Li, H. et al. 2D/3D heterojunction engineering at the buried interface towards high-performance inverted methylammonium-free perovskite solar cells. *Nat. Energy* **8**, 946–955 (2023).
 38. Lin, Y. et al. A Nd@C82-polymer interface for efficient and stable perovskite solar cells. *Nature* **642**, 78–84 (2025).
 39. Khenkin, M. V. et al. Consensus statement for stability assessment and reporting for perovskite photovoltaics based on ISOS procedures. *Nat. Energy* **5**, 35–49 (2020).
- X.Z. actively contributed to data analysis and discussions. E.H. and S.Cheng co-wrote the manuscript. C.T., Z.W., and T.B. revised the manuscript. All authors contributed to the discussion of the data.

Competing interests

The authors declare no competing interests.

Additional information

Supplementary information The online version contains supplementary material available at <https://doi.org/10.1038/s41467-026-70022-0>.

Correspondence and requests for materials should be addressed to Tongle Bu, Zhanhua Wei or Chengbo Tian.

Peer review information *Nature Communications* thanks Jianfeng Lu and the other, anonymous, reviewer(s) for their contribution to the peer review of this work. A peer review file is available.

Reprints and permissions information is available at <http://www.nature.com/reprints>

Publisher's note Springer Nature remains neutral with regard to jurisdictional claims in published maps and institutional affiliations.

Open Access This article is licensed under a Creative Commons Attribution-NonCommercial-NoDerivatives 4.0 International License, which permits any non-commercial use, sharing, distribution and reproduction in any medium or format, as long as you give appropriate credit to the original author(s) and the source, provide a link to the Creative Commons licence, and indicate if you modified the licensed material. You do not have permission under this licence to share adapted material derived from this article or parts of it. The images or other third party material in this article are included in the article's Creative Commons licence, unless indicated otherwise in a credit line to the material. If material is not included in the article's Creative Commons licence and your intended use is not permitted by statutory regulation or exceeds the permitted use, you will need to obtain permission directly from the copyright holder. To view a copy of this licence, visit <http://creativecommons.org/licenses/by-nc-nd/4.0/>.

© The Author(s) 2026

Acknowledgements

This work was financially supported by the National Natural Science Foundation of China [52472201 and U25A20234 (C.T.)], Natural Science Foundation of Fujian Province [2025J010037 (C.T.)], and the Promotion Program for Young and Middle-aged Teacher in Science and Technology Research of Huaqiao University [ZQN-806 (C.T.)]. We would like to thank the support of the Instrumental Analysis Center of Huaqiao University.

Author contributions

C.T. conceived the idea and supervised the work. E.H. and S.Cheng fabricated devices and analyzed the data. S.K. fabricated mini modules. E.H. performed XRD measurements and analyzed the data. S.Chen, Y.X., and S.Cheng performed MALDI-TOF-MS measurements and analyzed the data. Y.Q. performed the DFT calculations and analyzed the theoretical results. J.C. and X.C. contributed to the XPS test. J.Y., L.X., and